

Jia Liu

John A. Paulson School of Engineering and
Applied Sciences,
Harvard University,
Cambridge, MA 02138

Tianxiang Su

Schlumberger-Doll Research,
One Hampshire Street, MD-B353,
Cambridge, MA 02139

Nathan Wicks

Schlumberger-Doll Research,
One Hampshire Street, MD-B353,
Cambridge, MA 02139

Jahir Pabon

Schlumberger-Doll Research,
One Hampshire Street, MD-B353,
Cambridge, MA 02139

Katia Bertoldi

John A. Paulson School of Engineering and
Applied Sciences,
Harvard University,
Cambridge, MA 02138;
Kavli Institute,
Harvard University,
Cambridge, MA 02138

The Instability Mechanism of a Confined Rod Under Axial Vibrations

We studied the stability of a confined rod under axial vibrations through a combination of analytical and numerical analysis. We find that the stability of the system is significantly different than in the static case and that both the frequency and magnitude of the applied vibrational force play an important role. In particular, while larger vibrational forces always tend to destabilize the system, our analysis indicates that the effect of the frequency is not obvious and monotonic. For certain frequencies, a very small force is sufficient to trigger an instability, while for others the rod is stable even for large forces. Furthermore, we find that the stability of the confined rod is significantly enhanced by the presence of frictional contact and that in this case also the magnitude of the perturbation affects its response. [DOI: 10.1115/1.4031710]

Keywords: confined rod, axial vibration, instability, friction

1 Introduction

Motivated by tubing operations in the oilfield [1–3], there have been a number of studies on the stability of confined rods [4–20]. In fact, during insertion of a tubular rod into a horizontal wellbore frictional forces result in a buildup of compressive axial load that is often sufficient to trigger not only a sinusoidal mode but also helical buckling. At that point, because of the rapidly increasing contact force between the pipe and the well, lockup occurs, preventing further injection. In an effort to delay the onset of buckling and extend the reach, both passive [21–23] and active [24,25] methods have been investigated. In particular, axial vibrations generated by devices attached to one end of the tubing have been commonly used in the oil field to extend reach, as the elastic waves traveling along the rod have been shown to reduce the effective frictional load and therefore to delay the onset of buckling [26].

The effect of vibrations on the stability of mechanical systems has been the topic of many studies [27–30] and it is a paradigm in control theory that the stability of a pendulum can be completely altered by vibrations [31,32]. However, the mechanism by which axial vibrations affect the stability of a confined rod is currently not well understood. This is because the ability of a rod to both stretch and bend and the presence of frictional contact make the problem much more difficult.

Here, we combine analytical methods, numerical analysis, and dynamic simulations to investigate the buckling mechanism of a confined slender rod subjected to axial vibrations. We first show that in the absence of friction, the stability of such a rod is governed by Mathieu's equation [33] and that both the vibration amplitude and frequency affect the onset of buckling. Interestingly, we find that the effect of frequency is complex and not monotonic. For example, stable and unstable states may alternate when the vibration frequency is gradually increased and for

specific excitation frequencies the rod can lose stability even though the applied compressive force is significantly lower than the force required to trigger buckling in the static case. Moreover, for the case of frictional contact we also find that the onset of buckling is strongly affected by the amount of perturbation set by the environment, in agreement with observations recently reported for the static case [19].

The paper is organized as follows. After describing the system in Sec. 2, we investigate the stability of a constrained rod under axial vibrations in the case of frictionless contact (Sec. 3). In particular, we first derive the governing equation (Sec. 3.1), then numerically solve it using a leapfrog integration scheme (Sec. 3.2) and finally compare the results to those obtained performing dynamic simulations (Sec. 3.3), finding an excellent agreement. In Sec. 4, we then focus on the stability of an elastic constrained rod in the presence of frictional contact. Similarly, we first present the governing equation (Sec. 4.1), solve it numerically (Sec. 4.2), and then compare the results to those of dynamic simulations (Sec. 4.3).

2 A Confined Rod Under Axial Vibration

In this study, we consider an elastic rod of length L with a circular cross section of radius R_{rod} confined by a horizontal cylindrical channel of radius R_{channel} (Fig. 1) and investigate its stability when subjected to axial vibrations. We assume that the rod initially lays straight on the channel bottom due to gravity and study its stability when two axial forces of opposite direction $F = F_{\text{ave}} + dF \sin(\omega t)$ are applied at both of its ends. In particular, we determine for which combinations of $(F_{\text{ave}}, dF, \text{ and } \omega)$ the rod buckles and takes a wavy configuration described by the deflection angle $\theta(s, t)$, which is a function of arc length s and time t .

3 Instability Analysis for the Frictionless Case

In this section, we first derive the partial differential equation (PDE) which governs the stability of the rod (Sec. 3.1) and then

Manuscript received September 4, 2015; final manuscript received September 29, 2015; published online October 20, 2015. Editor: Yonggang Huang.

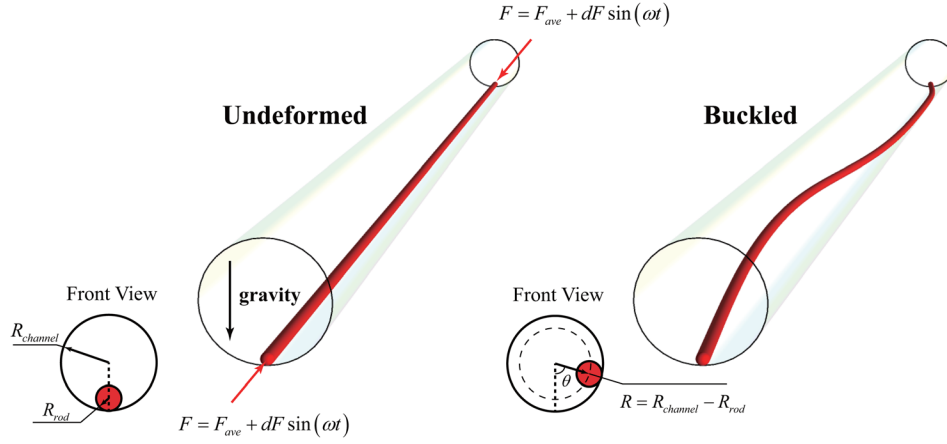


Fig. 1 Schematic of a confined rod in a cylindrical channel. Two identical axial forces with opposite direction, $F = F_{ave} + dF \sin(\omega t)$, are applied to its ends. When buckling occurs, the rod takes a wavy configuration.

solve it numerically using a leapfrog integration scheme (Sec. 3.2). Finally, we compare the results with those obtained performing dynamic simulations (Sec. 3.3).

3.1 Governing Equation. To identify the onset of instability for the case of frictionless contact, we start by determining the Euler–Lagrange equation for our system. If we assume that the period of the excitation force is much larger than the time for an axial wave to travel through the rod (i.e., $\sqrt{E/\rho} \gg \omega L/2\pi$, E and ρ denoting the Young’s modulus and density of the material, respectively), the axial force in the rod can be treated as uniform through the rod and by minimizing the Lagrangian of the system, its governing equation is obtained as [19]

$$\rho A \frac{\partial^2 \theta}{\partial t^2} + EI \frac{\partial^4 \theta}{\partial s^4} + [F_{ave} + dF \sin(\omega t)] \frac{\partial^2 \theta}{\partial s^2} + \frac{\rho A g \theta}{R} = 0 \quad (1)$$

where $R = R_{channel} - R_{rod}$ and A and EI denote the cross-sectional area and bending rigidity of the rod, respectively. To study the stability of the rod, we first decompose θ into Fourier series

$$\theta(s, t) = \sum_{m=1}^{\infty} A_m(t) \sin(\omega_m s) \quad (2)$$

where $\omega_m = m\pi/L$. Substitution of Eq. (2) into Eq. (1) yields the governing equation for the Fourier modes

$$\frac{\partial^2 A_m}{\partial \tau^2} = (\beta_m + \alpha_m \sin \tau) A_m, \quad m = 1, 2, \dots, \infty \quad (3)$$

where $\tau = \omega t$ and

$$\alpha_m = \frac{\omega_m^2 dF}{\rho A \omega^2} \quad (4)$$

$$\beta_m = -\left(\frac{EI \omega_m^4}{\rho A \omega^2} + \frac{g}{\omega^2 R} - \frac{F_{ave} \omega_m^2}{\rho A \omega^2} \right)$$

Equation (3) is the well-known Mathieu’s equation [33] and indicates that the stability of the m th mode in case of frictionless contact only depends on the two parameters α_m and β_m and not on the initial conditions.¹

¹Although the rigorous proof of the fact that the stability of the m th mode is not affected by the initial conditions involves the Floquet’s theorem [34–36], it can be intuitively seen by noting that the solution of Eq. (3) does not change when A_m is multiplied by an arbitrary constant.

Note that in the limit of an axial force applied statically (i.e., $dF = 0$), α_m vanishes and Eq. (3) reduces to

$$\frac{\partial^2 A_m}{\partial \tau^2} - \beta_m A_m = 0, \quad m = 1, 2, \dots, \infty \quad (5)$$

so that $\beta_m = 0$ identifies the onset of instability for the m th mode [19]. In fact, if the linearized system described by Eq. (5) is perturbed and $\beta_m > 0$, the magnitude of the initial perturbation grows exponentially with time. However, this conclusion is not true anymore in the presence of axial vibrations ($\alpha_m > 0$).

3.2 Numerical Solution of the PDE. To investigate the stability of the m th mode of the rod, we start by solving numerically Eq. (3) (Note that an analytical solution of Eq. (3) can also be derived—see Appendix). In particular, we implemented a classic leapfrog integration scheme [37] and updated A_m incrementally, using a small time increment ($d\tau = 5 \times 10^{-4}$) to ensure that the solution does not diverge because of numerical instabilities. More specifically, we assigned zero displacement ($A_m(0) = 0$) and an initial nonzero velocity ($A'_m(0) = \epsilon$) as initial conditions and monitored the evolution of A_m . If the m th mode is stable, A_m remains bounded within a small interval; by contrast, when it is unstable, A_m grows indefinitely as a function of time. Operationally, the m th mode of the system is considered to be stable if after 100 cycles

$$\frac{A_m(200\pi)}{A'_m(0)} < 1 \times 10^6 \quad (6)$$

To numerically explore the influences of α_m and β_m , we solved Eq. (3) 10,000 times for different combinations of $\alpha_m \in [0, 6]$ and $\beta_m \in [-4, 3]$ and determined the stability of each point using Eq. (6). We then report the stable modes using a red marker in Fig. 2(a). As expected, in the limit of the load applied statically (i.e., $\alpha_m = 0$), the m th mode is unstable for $\beta_m > 0$. However, as the load is applied dynamically, the axial vibrations significantly affect the stability of the system, even for very small values of α_m . Interestingly, the effect of axial vibrations is not obvious and monotonic. For example, for $\beta_m = -0.25$, an increase in α_m as small as 1×10^{-8} is enough to make the m th mode unstable. By contrast, for $\beta_m = -0.80$, the m th mode is stable up to $\alpha_m = 1.5$. Additionally, the results reported in Fig. 2(a) indicate that for specific dynamic conditions, a mode can be stable even for $\beta_m > 0$. Interestingly, this means that in some rare cases the axial vibrations can stabilize a given mode.

Although the results reported in Fig. 2(a) can be easily used to determine the stability of the m th mode of an elastic rod under

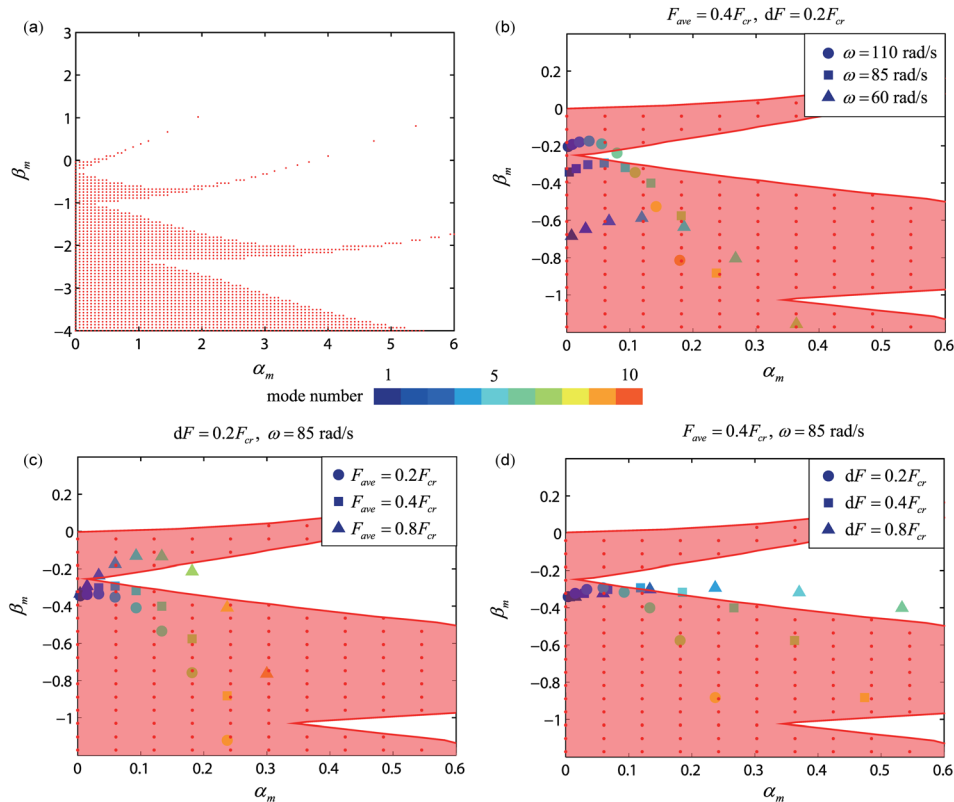


Fig. 2 Stability map obtained by solving Eq. (3) numerically. (a) The markers indicate the stable configurations as determined by solving numerically the PDE. (b)–(d) First 10 modes for a Nitinol rod superimposed on the stability map, when we varied (b) ω , (c) F_{ave} , and (d) dF . The shape of the markers indicates a specific set of loading conditions, while their color represents the mode number.

specific loading conditions, it is not trivial to use them to infer whether the system is stable or not. In fact, this requires checking whether all modes are stable. To more easily identify the loading conditions (compression force, F_{ave} , vibration force, dF , and vibration frequency, ω) resulting in unstable configurations, we focus on a lab setup consisting of a Nitinol rod confined by a poly-plastic channel, which has recently been used to investigate the buckling and post-buckling behavior of an elastic rod injected into a horizontal, frictional, and cylindrical constraint [20]. The rod has a Young's modulus $E = 68$ GPa, density $\rho = 6500$ kg/m³, radius $R_{rod} = 0.8$ mm, and length $L = 3.1$ m. Moreover, the channel has radius $R_{channel} = 9.4$ mm. For such confined rod, the critical force under static uniaxial compression is given by $F_{cr} = 2\sqrt{EI\rho Ag/R} = 1.70$ N and the corresponding critical mode is $m_{cr} = [\rho AgL^4/(\pi^4 REI)]^{1/4} = 6$ [4].

We start to investigate the effect of the loading conditions on the stability of the rod keeping two loading parameters constant and varying the third one. In particular, in Figs. 2(b)–2(d) we report with markers the first ten modes of the rod when we varied ω , F_{ave} , and dF , respectively. Note that the shape of the markers indicates a specific set of loading conditions, while their color represents the mode number. As expected from Eq. (4), α_m increases monotonically with the mode number. On the other hand, as the mode number increases, β_m is found to increase, reach a maximum, and then decrease. Focusing on Fig. 2(b), we find that for $\omega = 60$ rad/s (triangular markers) and $\omega = 85$ rad/s (square markers), all modes stay within the stable region, indicating a stable configuration of the rod. By contrast, for $\omega = 110$ rad/s (circular markers) there is one mode (the sixth mode) which lies outside the stable zone, so that the rod is unstable. Similar trends are observed when F_{ave} and dF are varied, as shown in Figs. 2(c) and 2(d). Although these results do not provide a complete stability

map, they indicate that by increasing either ω or F_{ave} or dF the system may become unstable, since some of the modes fall outside the numerically determined stable region (shaded area). Finally, we note that we were not able to identify a stable rod with a mode characterized by $\beta_m > 0$.

To further explore the stability of the rod, in Figs. 3(a)–3(d) we indicate with markers all stable configurations in the ω – F_{ave} space for $dF = 0.1, 0.2, 0.3$, and $0.5 F_{cr}$. Note that the maps are determined numerically by checking the first 25 modes. Although this criterion is empirical, its accuracy was ensured by comparing the results with those obtained by checking the stability of more modes.

As expected, the maps shown in Figs. 3(a)–3(d) indicate that by increasing the amplitude of the vibrational force, dF , the system tends to be more unstable. For example, for $dF = 0.1F_{cr}$ (Fig. 3(a)), most of the loading conditions with $F_{ave} < F_{cr}$ result in stable configurations. This is expected since as $dF \rightarrow 0$, the rod is always stable for $F_{ave} < F_{cr}$. However, if dF is increased to $0.5F_{cr}$ the stable domain dramatically shrinks and becomes limited to a small region characterized by low frequencies and low static compressive forces.

Interestingly, Fig. 3(a) also indicates that the effect of the frequency ω is not obvious and monotonic. In fact, given a certain value of dF , for some frequencies the rod is stable even for large compressive forces, while for other frequencies the instability is triggered for very low values of F_{ave} . As an example, for $dF = 0.2F_{cr}$ (Fig. 3(b)) the rod is immediately unstable when $\omega \sim 120$ rad/s. By contrast, for $\omega \sim 20$ rad/s a compressive force $F_{ave} = 0.8F_{cr}$ needs to be applied to trigger the instability. We also note that for $\omega > 110$ rad/s, the stable and unstable regimes alternate, indicating that for some frequencies the onset of instability can be delayed by increasing the compressive forces F_{ave} .

To further study the effect of ω and F_{ave} on the stability of the rod, we consider $dF = 0.2F_{cr}$ and focus on two frequencies,

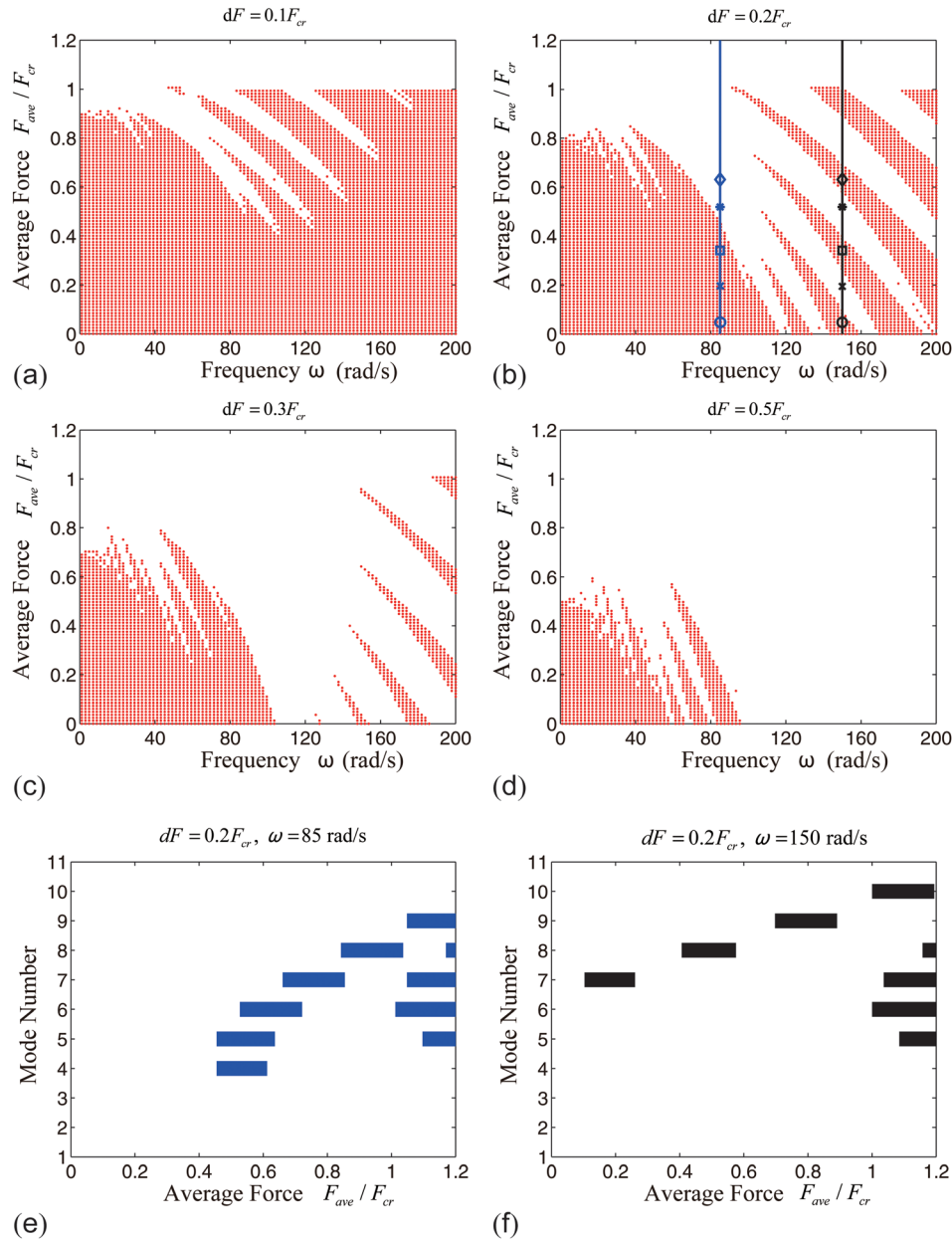


Fig. 3 (a)–(d) Numerically obtained stability maps for a Nitinol rod when (a) $dF = 0.1F_{cr}$, (b) $dF = 0.2F_{cr}$, (c) $dF = 0.3F_{cr}$, and (d) $dF = 0.5F_{cr}$. All stable configurations are indicated by dots. (e) and (f) Evolution of the unstable modes as a function of F_{ave} for $dF = 0.2F_{cr}$. Results for both (e) $\omega = 85$ rad/s and (f) $\omega = 150$ rad/s are reported.

$\omega = 85$ rad/s (left vertical line in Fig. 3(b)) and $\omega = 150$ rad/s (right vertical line in Fig. 3(b)). In Figs. 3(e) and 3(f), we use colored pixels to indicate the evolution of the unstable modes as a function of F_{ave} for these two frequencies. The results again clearly show that the frequency of the excitation affects the stability of the system. In fact, for $\omega = 85$ rad/s (Fig. 3(e)) all modes are stable for $F_{ave} < 0.45F_{cr}$, while we find at least one unstable mode for $F_{ave} > 0.45F_{cr}$. By contrast, for $\omega = 150$ rad/s an alternation of stable and unstable configurations is found when F_{ave} is progressively increased. In fact, the rod is stable for $F_{ave} = 0.05, 0.34$, and $0.63 F_{cr}$, but unstable for $F_{ave} = 0.20$ and $0.52 F_{cr}$. Finally, we also note that the unstable modes are always close to the critical mode under static loading (in this case $m_{cr} = 6$), but change as the applied force F_{ave} is increased.

3.3 Dynamic Simulations. Next, we perform dynamic simulations and compare the results with the predictions from our

analysis. Following an approach that has been previously successfully applied to study the stability of frictionally confined rods [19], the rod (with the same geometric and material properties as those described in Sec. 3.2) is discretized into segments (in this case 250 segments), each of which is characterized by its position and orientation. To obtain the deformed configuration of the rod, we apply a step-by-step integration scheme (computation time step $dt = 2.5 \mu s$). At each computational time step, the extension, bending, twisting, and shear strains are computed for each segment using the current position and orientation of the rod following the Kirchhoff model [38]. The stresses along the rod are then computed from these strains, assuming an isotropic linear elastic material. The force loading on each segment, acceleration of the segments, and the positions for the next time step are then successively updated. Additionally, the channel is modeled as a visco-elastic frictional contact using a modified Hertzian contact formulation [39,40].

To compare the results of the dynamic simulations with those reported in Fig. 3, we set the rod initially straight and statically load it by applying a prestrain $\epsilon_{pre} = F_{ave}/(EA)$. Then, we assign to each node a random initial transverse velocity and apply two axial forces of magnitude $dF \sin(\omega t)$ to the ends of the precompressed rod. Each simulation is run until $t = 2$ s and we monitor the evolution of the rod. Note that, if buckling occurs, it typically happens within 50 ms and results in an increasing amplitude for the displacements of the nodes. Practically, the rod is judged to be unstable if the maximum angle θ for all nodes exceeds 0.087 rad (5 deg) after 1 s.

In Fig. 4, we report numerical snapshots showing a top view of the deformed rod at $t = 1.5$ s. All results are obtained for $dF = 0.2F_{cr}$ and two representative frequencies, $\omega = 85$ rad/s (Fig. 4(a)) and $\omega = 150$ rad/s (Fig. 4(b)). Moreover, five different values of dF/F_{cr} are considered, also highlighted with markers in Fig. 3(b). Remarkably, we find an excellent agreement between the predictions of our analysis and the results of the dynamic simulations. In fact, for all loading conditions that were predicted to result in unstable configurations in Fig. 3(b), we find that the rod buckles and takes a wavy configuration. Additionally, for the loading conditions that were predicted to result in stable configurations in Fig. 3(b), the rod is still straight at $t = 1.5$ s. We also notice that as previously observed for the static case [19], typically one mode dominates at instability, resulting in a periodic wavy pattern, even though random initial velocities are assigned as imperfections.

4 Instability Analysis for the Friction Case

Following an approach similar to that used for the analysis of the frictionless case, in this section we start by presenting the equation governing the stability of a confined rod in the presence of frictional contact (Sec. 4.1). We then integrate it numerically (Sec. 4.2) and finally compare the results with those obtained performing dynamic simulations (Sec. 4.3).

4.1 Governing Equation. In the presence of dry friction, the governing equation is

$$\rho A \frac{\partial^2 \theta}{\partial t^2} + EI \frac{\partial^4 \theta}{\partial s^4} + [F_{ave} + dF \sin(\omega t)] \frac{\partial^2 \theta}{\partial s^2} + \frac{\rho A g \theta}{R} - \frac{F_{fric}(s, t)}{R} = 0 \quad (7)$$

with

$$|F_{fric}(s, t)| \leq \mu_\theta(s, t) N \quad (8)$$

where N is the normal contact force and $\mu_\theta(s, t)$ is the transverse component of the friction coefficient μ . Moreover, we note that Eq. (8) can be simplified to

$$F_{fric}(s, t) = -\mu_\theta(s, t) N \text{sign}\left(\frac{\partial \theta}{\partial t}\right) \quad (9)$$

since the rod is always moving axially because of the applied vibrations (except for a few instants when parts of the rod are at rest).

Assuming small values for θ , which is sufficient for our goal of identifying the buckling onset, the contact force can be approximated as the gravity force

$$N = \rho A g \quad (10)$$

since the centripetal force can be neglected given that $\partial \theta / \partial t$ is small.

To investigate the stability of the system, we assume that at the onset of instability only one mode (the m th mode) dominates [19], so that

$$\theta \approx A_m(t) \sin(\omega_m s) \quad (11)$$

and

$$\text{sign}\left(\frac{\partial \theta}{\partial t}\right) \approx B_m(t) \sin(\omega_m s) \quad (12)$$

where the coefficient $B_m(t)$ is obtained as

$$B_m(t) \approx \frac{2}{L} \int_0^L \text{sign}\left[\frac{\partial A_m}{\partial t} \sin(\omega_m s)\right] \sin(\omega_m s) ds = \frac{4}{\pi} \text{sign}\left(\frac{\partial A_m}{\partial t}\right) \quad (13)$$

Substituting Eqs. (11), (12), and (13) into Eq. (7), the governing equation for the dominant m th Fourier mode in the case of frictional contact is obtained as

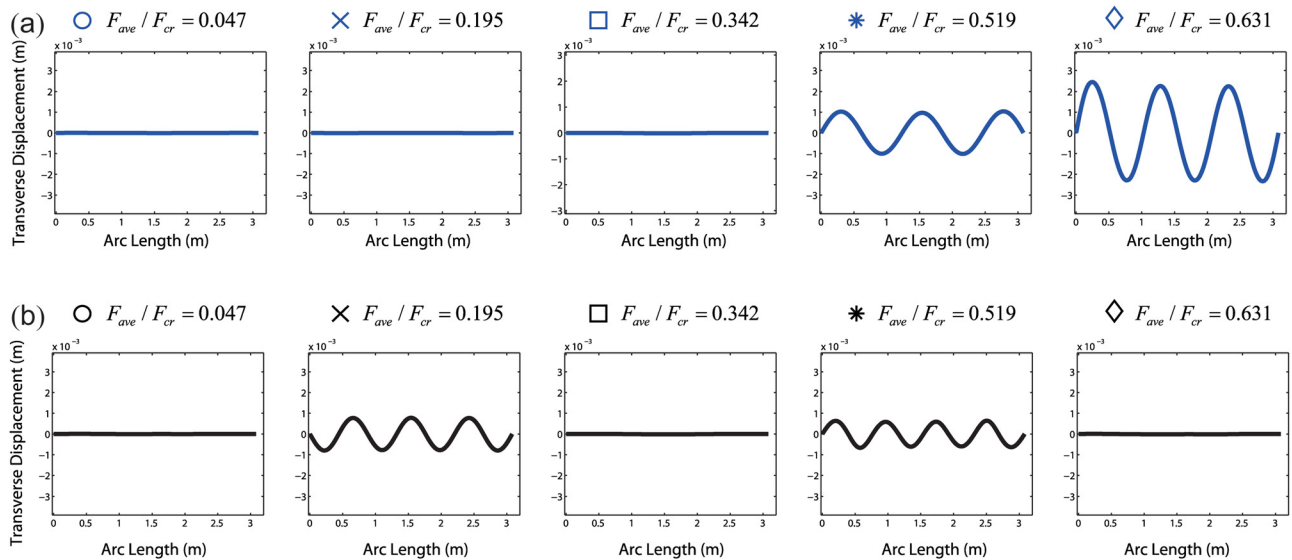


Fig. 4 Numerical top-view snapshots showing the configurations of the rod at $t = 1.5$ s, as obtained from the dynamic simulations for (a) $\omega = 85$ rad/s and (b) $\omega = 150$ rad/s. All simulated loading conditions are indicated by a marker in Fig. 3(b).

$$\frac{\partial^2 A_m}{\partial \tau^2} = (\beta_m + \alpha_m \sin \tau) A_m - \gamma \operatorname{sign} \left(\frac{\partial A_m}{\partial \tau} \right) \quad (14)$$

where α_m and β_m are the same parameters defined in Eq. (4) and

$$\gamma = \frac{4\mu_\theta g}{\pi\omega^2 R} \quad (15)$$

Note that μ_θ in Eq. (15) is a function of both the arc length and time (i.e., $\mu_\theta = \mu_\theta(s, t)$). In fact, while the friction coefficient μ is a constant, its transverse component μ_θ depends on the ratio between the axial and transverse velocity. Therefore, to solve Eq. (14), the axial velocity also needs to be known. However, since the stability of the rod is affected by the global conditions experienced by the system, in our study we assume that μ_θ is constant and given by

$$\mu_\theta = \mu \frac{\bar{v}_\theta}{\sqrt{\bar{v}_a^2 + \bar{v}_\theta^2}} \quad (16)$$

where \bar{v}_a and \bar{v}_θ are the averaged axial and transverse velocity components. In particular, since the averaged axial displacement experienced by the rod over half a cycle is $2/L \int_0^{L/2} 2dF/(EA) \cdot x dx = LdF/(2EA)$, the averaged axial velocity is given by

$$\bar{v}_a = \frac{LdF}{2EA} \cdot \frac{\omega}{\pi} \quad (17)$$

Moreover, since the instability is typically triggered during the first few loading cycles, we use the initial assigned transverse velocity ϵ to estimate \bar{v}_θ as

$$\bar{v}_\theta = v_\theta(0) = \omega R \epsilon \quad (18)$$

4.2 Numerical Solution of the PDE. We start by solving Eq. (14) numerically using the leapfrog integration scheme described in Sec. 3.2. In all our calculations, we assume a nonzero initial velocity ($A'_m(0) = \epsilon$) and a vanishing initial displacement ($A_m(0) = 0$), but we do not expect the results to be affected by this particular choice of initial conditions [19]. Differently from the frictionless case, Eq. (14) indicates that in the presence of friction the stability of the m th mode is controlled not only by α_m and β_m but also by the friction parameter γ and the magnitude of the initial velocity ϵ . Therefore, in Fig. 5 we report four stability maps obtained assuming a constant friction term $\gamma = 0.01$ and varying ϵ from 0.005 to 0.5. Interestingly, we find that friction significantly enhances the stability of the modes. In fact, for small values of the initial perturbation ϵ , the modes are typically stable even for $\beta_m > 0$. However, as the perturbation ϵ is gradually increased the stable domain progressively shrinks and for $\epsilon > 0.05$ it is almost the same as that found in the frictionless case (Fig. 2). Similar trends can be observed also when the perturbation ϵ is kept constant and the friction term γ is varied. For small values of γ , the behavior of the system resembles that found in the frictionless case, while for large values of γ the stable domain is significantly enlarged. Note that these observations are well aligned with the findings previously reported for a constrained rod axially compressed [19].

Next, we explicitly determine the loading conditions that result in an instability for a rod with the same properties as those presented in Sec. 3.2 when $\mu = 0.1$. The stability maps shown in Figs. 6(a)–6(d) highlight again the fact that the magnitude of the perturbation (here represented by the initial velocity) has a crucial effect on the stability of the system. For $v_\theta(0) = 30$ mm/s, most of the considered loading conditions are stable, while for $v_\theta(0) = 50$ mm/s the stable domain contracts dramatically. Moreover, we note that the effect of the vibration force dF and the frequency ω on the stability of the system is similar to that previously observed for the frictionless case. In fact, as for the

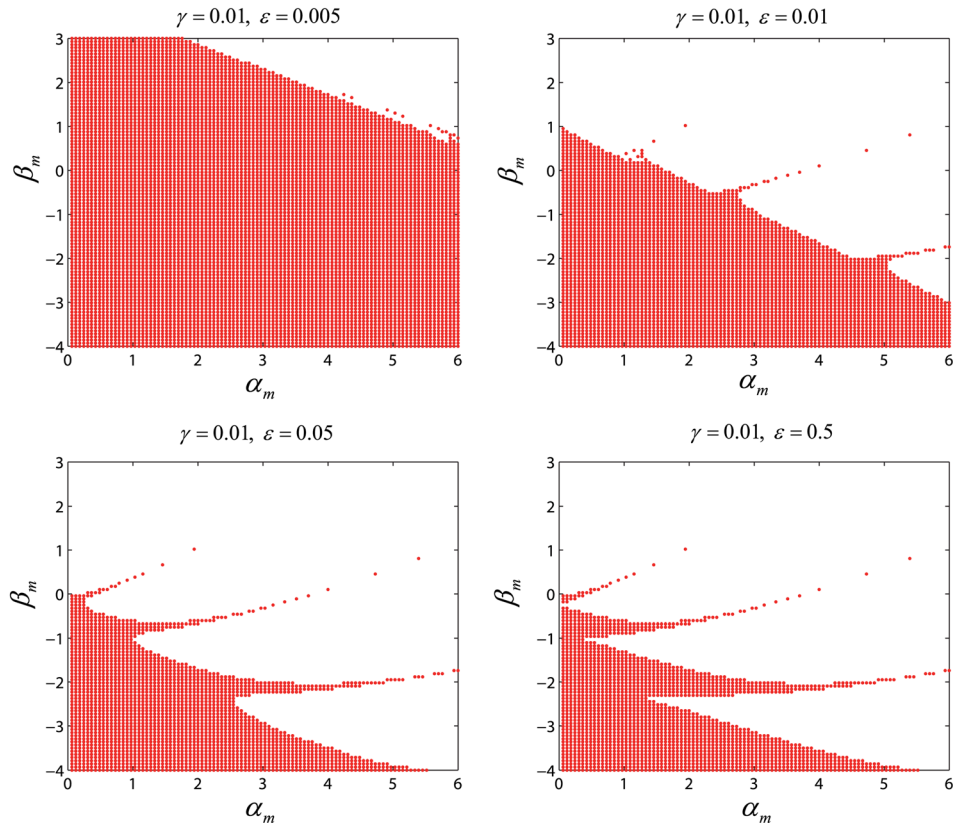


Fig. 5 Stability maps obtained by solving Eq. (14) numerically. The friction term γ is kept constant while the perturbation ϵ is varied from 0.005 to 0.5.

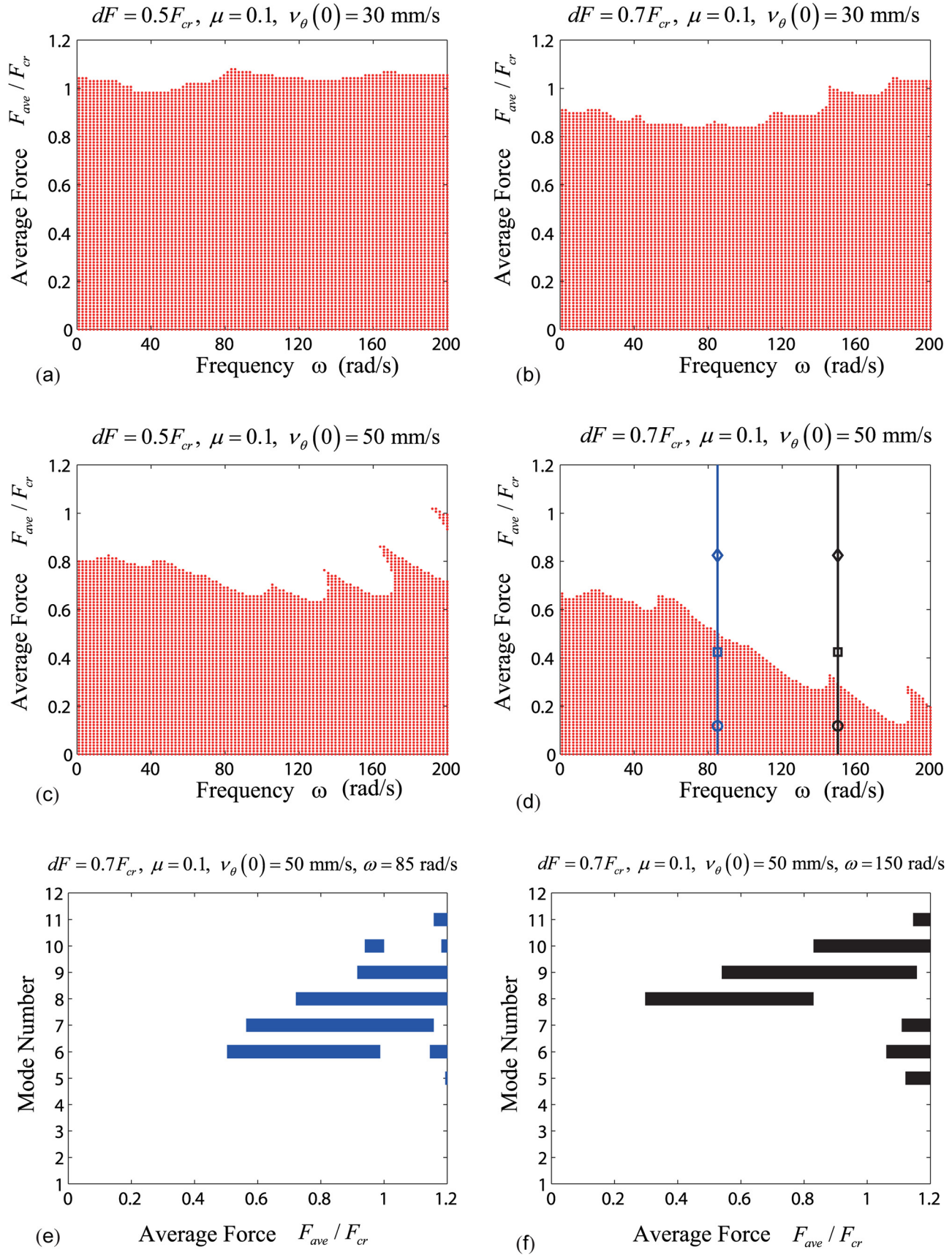


Fig. 6 (a)–(d) Numerically obtained stability maps for a Nitinol rod in the presence of frictional contact ($\mu = 0.1$) when (a) $dF = 0.5F_{cr}$ and $v_\theta(0) = 30$ mm/s, (b) $dF = 0.7F_{cr}$ and $v_\theta(0) = 30$ mm/s, (c) $dF = 0.5F_{cr}$ and $v_\theta(0) = 50$ mm/s, and (d) $dF = 0.7F_{cr}$ and $v_\theta(0) = 50$ mm/s. All stable configurations are indicated by dots. (e) and (f) Evolution of the unstable modes as a function of F_{ave} for $dF = 0.7F_{cr}$ and $v_\theta(0) = 50$ mm/s. Results for both (e) $\omega = 85$ rad/s and (f) $\omega = 150$ rad/s are reported.

frictionless case, an increase in dF is found to reduce the stable domain, while ω has a more complicated effect on the stability of the system. It is interesting to observe that in the presence of friction the effect of larger values of ω is more pronounced than in the frictionless case, since Eq. (17) indicates that higher frequencies result in larger axial velocities and, therefore, smaller transverse friction components (Eq. (16)). Moreover, differently from the case of frictionless contact (Fig. 3), when friction is present we do not see alternation of stable and unstable configurations as F_{ave} is increased while keeping ω constant.

As in the frictionless case, when the system is unstable, typically several modes, which are close to the critical mode predicted in the static case, are unstable. To highlight this point in Figs. 6(e) and 6(f), we report the unstable modes as a function of F_{ave} for $\omega = 85$ rad/s and $\omega = 150$ rad/s.

4.3 Dynamic Simulations. Next, we conduct dynamic simulations using the method described in Sec. 3.3 and compare the results to the numerical solution of the PDE. Additionally, friction is implemented using Coulomb's law with the static and dynamic friction coefficients set to be the same (i.e., $\mu = \mu_s = \mu_d$).

In Fig. 7, we report simulation snapshots showing a top view of the deformed rod at $t = 4$ s (note that in the case of frictional contact, the simulations are run for a longer time to minimize the effect of the relatively large applied initial imperfections). All results are obtained for $dF = 0.7F_{cr}$ and $v_\theta(0) = 50$ mm/s. Moreover, two frequencies $\omega = 85$ rad/s (Fig. 7(a)) and $\omega = 150$ rad/s (Fig. 7(b)) and three different values of F_{ave}/F_{cr} (also highlighted with markers in Fig. 6(d)) are considered.

Since our analysis indicates that in the case of frictional contact, the stability of the rod is highly affected by the perturbation set by the environment, we consider four different sets of initial conditions:

- **Case A:** We impose the same initial conditions as those considered in our analysis and assign to each node an initial transverse velocity

$$v_\theta(x, 0) = v_\theta(0) \sin\left(m_{cr} \frac{x}{L}\right) \quad (19)$$

where x denotes the initial position of the node along the rod and m_{cr} is one of the unstable modes predicted by the numerical

solutions of the PDE (see Figs. 6(e) and 6(f)). In particular, we choose $m_{cr} = 6$ for $\omega = 85$ rad/s and $m_{cr} = 8$ for $\omega = 150$ rad/s.

- **Case B:** To test whether the assumption of a single mode dominating at the onset of instability is valid, we consider the perturbation to be the superposition of several modes and assign to each node an initial transverse velocity

$$v_\theta(x, 0) = v_\theta(0) \left[\sin\left(4\frac{x}{L}\right) + \sin\left(6\frac{x}{L}\right) + \sin\left(8\frac{x}{L}\right) + \sin\left(10\frac{x}{L}\right) \right] \quad (20)$$

- **Case C:** To further study the role played by the interactions between different modes, we assign to each node an initial transverse velocity

$$v_\theta(x, 0) = v_\theta(0) \sin\left(m \frac{x}{L}\right) + v_\theta^{\text{random}} \sum_{\substack{k=1 \\ k \neq m}}^{15} \sin\left(k \frac{x}{L}\right) \quad (21)$$

where $v_\theta^{\text{random}} \in [-v_\theta(0), v_\theta(0)]$ is a random number. Note that we use $m = 6$ and 10 for $\omega = 85$ rad/s and $m = 8$ and 10 for $\omega = 150$ rad/s.

- **Case D:** Since in reality the perturbation experienced by the rod is random, we assign to each node an initial transverse velocity

$$v_\theta(x, 0) = v_\theta^{\text{random}} \quad (22)$$

As predicted by our analysis, the results reported in Fig. 7 indicate that, when the compressive force F_{ave} is small ($F_{ave} = 0.118F_{cr}$), the rod is stable for both $\omega = 85$ rad/s and $\omega = 150$ rad/s. We also see that in this case, the type of perturbation set by the environment does not affect the response of the system, since the rod is found to be stable for all considered sets of initial conditions.

When the applied compressive force is increased to $F_{ave} = 0.424F_{cr}$, our analysis predicts a stable configuration for $\omega = 85$ rad/s and an unstable one for $\omega = 150$ rad/s. Although all simulations predict a stable configuration for $\omega = 85$ rad/s, we find that for $\omega = 150$ rad/s the instability of the rod is not captured if the initial velocity distribution is assigned as in case C with $m = 10$ and as in case D. This is because the magnitude of the

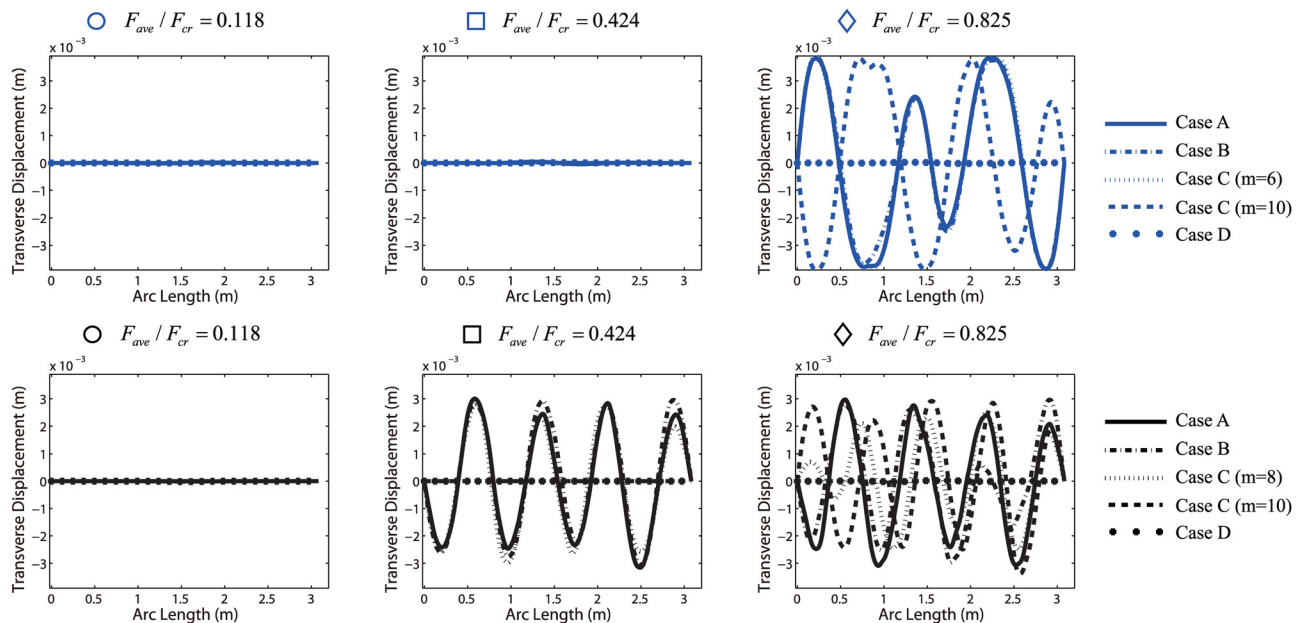


Fig. 7 Numerical top-view snapshots showing the configurations of the rod at $t = 4$ s, as obtained from the dynamic simulations for (a) $\omega = 85$ rad/s and (b) $\omega = 150$ rad/s. All simulated loading conditions are indicated by a marker in Fig. 6(d).

unstable mode ($m=8$) contained into these perturbations is lower than $v_0(0) = 50$ mm/s and therefore not large enough to trigger the instability. On the other hand, for cases A, B, and C with $m=8$, the simulations predict the rod to be unstable and we find that mode 8 is always the one growing, indicating that the effect of mode interaction is not significant and that typically one mode grows and dominates if instability occurs.

For $F_{ave} = 0.825F_{cr}$, the analysis predicts unstable configurations for both $\omega = 85$ rad/s and $\omega = 150$ rad/s. In this case, we find that all dynamic simulations except those performed using purely random initial velocity distributions (case D) result in unstable configurations. For $\omega = 85$ rad/s, the rod always buckles into mode 6, although its shape is slightly affected by the initial conditions. Interestingly, for $\omega = 150$ rad/s mode 8 is found to grow for cases A and B, while mode 9 dominates for case C (with both $m=8$ and $m=10$). This indicates that when multiple modes are unstable (in this case, modes 8 and 9 are both unstable), the interaction between them may play a role and affect the final configuration of the rod.

Finally, it is important to point out that we monitor the torsional and shear energy in all our simulations and observe that their contribution is negligible compared to that of the bending and stretching energies (it is typically less than 2% of the total energy even for very large post-buckling deformations). This observation thus confirms the validity of our analysis, where the contribution from shear and torsion has been neglected.

5 Conclusion

We have used a combination of analysis and dynamic simulations to study the stability of a confined rod under axial vibrations. Interestingly, we have found that the vibrations significantly affect the response of the system. In fact, both the critical modes and forces are different from those found in the static case and depend on both the frequency and magnitude of the vibrational force. Moreover, for the case of frictional contact, also the magnitude of the perturbation set by the environment affects the onset of the instability. While larger values of friction coefficients enhance the stability of the system, by increasing the amount of perturbation the onset of instability is triggered earlier.

Importantly, our analysis indicates that axial vibrations may not always help in delaying buckling and lockup in the oil field. While it has been previously shown that axial vibrations can reduce the effective friction coefficient between the tubing and the wellbore [24], our study shows for certain vibration conditions, the tubing buckles for very low values of compressive axial load. Therefore, it is worthwhile to study further the effect of the vibration parameters when the injection process is considered.

Finally, we note that the goal of our analysis is to capture the onset of the first bifurcation, so that simplified governing equations under the assumption of small deformations can be used. Different rod models that fully account for its large deformation, such as the Cosserat beam model [41] and the Kirchhoff rod model [42], should be used to capture secondary bifurcations (e.g., helical lock-up) encountered along the loading path [11,13,16,17].

Appendix: The Approximate Analytical Solution for Mathieu's Equation, Eq. (3)

In this appendix, we compare the numerical solution of Mathieu's equation presented in Sec. 3.2 (Fig. 2) with its analytical solution.

A well-known and accurate method to determine the boundaries between the stable and unstable regions is based on the Hill's determinants [43–46]. This approach is based on the fact that, according to the Floquet theory [34,35], the bounded solution along the boundaries has a period of 2π or 4π and thus can generally be expressed as a Fourier series [47]

$$A_m(\tau) = a_0 + \sum_{k=1}^{+\infty} \left[a_k \cos\left(\frac{k\tau}{2}\right) + b_k \sin\left(\frac{k\tau}{2}\right) \right] \quad (A1)$$

where a_k and b_k are the Fourier coefficients. Introducing Eq. (A1) into Eq. (3) and employing the principle of harmonic balance, four sets of algebraic equations are obtained

$$\begin{aligned} \frac{1}{4} \begin{bmatrix} 1 + 4\beta_m & 2\alpha_m & 0 & 2\alpha_m & 0 & 0 & \dots \\ 0 & -2\alpha_m & 9 + 4\beta_m & 0 & 0 & 2\alpha_m & \dots \\ \dots & \dots & \dots & \dots & \dots & \dots & \dots \end{bmatrix} \mathbf{x} &= 0 \\ \frac{1}{4} \begin{bmatrix} 2\alpha_m & 1 + 4\beta_m & 0 & -2\alpha_m & 0 & 0 & \dots \\ 2\alpha_m & 0 & 0 & 9 + 4\beta_m & -2\alpha_m & 0 & \dots \\ \dots & \dots & \dots & \dots & \dots & \dots & \dots \end{bmatrix} \mathbf{x} &= 0 \\ \frac{1}{2} \begin{bmatrix} 2\beta_m & 0 & \alpha_m & 0 & 0 & 0 & \dots \\ 0 & 2 + 2\beta_m & 0 & 0 & -\alpha_m & 0 & \dots \\ \dots & \dots & \dots & \dots & \dots & \dots & \dots \end{bmatrix} \mathbf{y} &= 0 \\ \frac{1}{2} \begin{bmatrix} 2\alpha_m & 0 & 2 + 2\beta_m & -\alpha_m & 0 & 0 & \dots \\ 0 & \alpha_m & 0 & 0 & 8 + 2\beta_m & -\alpha_m & \dots \\ \dots & \dots & \dots & \dots & \dots & \dots & \dots \end{bmatrix} \mathbf{y} &= 0 \end{aligned} \quad (A2)$$

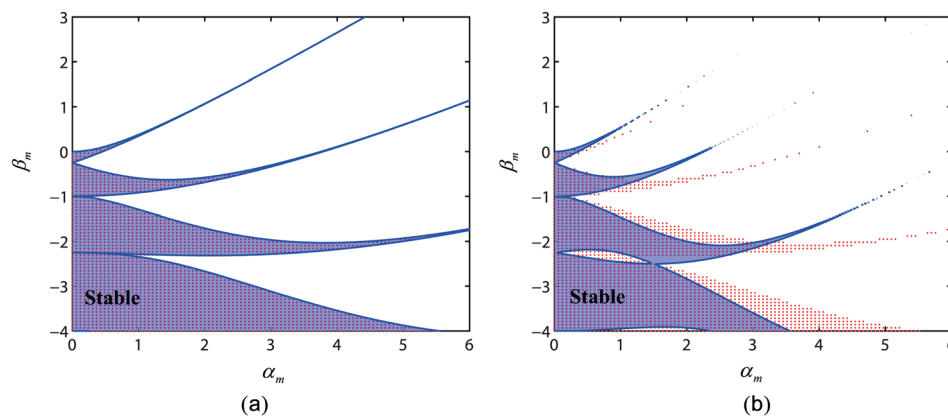


Fig. 8 Stability maps obtained by solving Eq. (3) analytically and numerically. The shaded areas indicate the stable domains as predicted by the analytical solution obtained using (a) the method of Hill's determinants and (b) the simplified method in which the sinusoidal functions are approximated as square waves, while the markers indicate the stable configurations as determined by solving numerically the PDE.

with

$$\mathbf{x} = (a_1, b_1, a_3, b_3, \dots)^T \quad \text{and} \quad \mathbf{y} = (a_0, a_2, b_2, a_4, b_4, \dots)^T \quad (\text{A3})$$

The Fourier coefficients a_k and b_k can then be solved by setting to zero the determinants of the four matrices in Eq. (A2), known as the Hill's infinite determinants. To limit the computational cost, in our calculations we consider the first 40 terms in the Fourier series (A1) (yielding to 40×40 and 41×41 matrices). In Fig. 8(a), we report the stability map for the m th mode obtained by solving Eq. (3) analytically using the method of Hill's determinants (shaded area) and numerically (markers) and find an excellent agreement.

We also note that simplified approaches resulting in explicit expressions for the boundaries of the stable zones can be used to solve the Mathieu equation. In particular, by exploiting Floquet theory and approximating the sinusoidal functions with square waves [36], the domain within which the m th mode is stable can be quantified as [36]

$$\left| 2 \cos(\pi q_m) \cosh(\pi p_m) + \left(\frac{p_m}{q_m} - \frac{q_m}{p_m} \right) \sin(\pi q_m) \sinh(\pi p_m) \right| < 2 \quad (\text{A4})$$

where $q_m = \sqrt{\alpha_m - \beta_m}$ and $p_m = \sqrt{\alpha_m + \beta_m}$. Note that Eq. (A4) is valid only for $\alpha_m > \beta_m$. In fact, for $\alpha_m < \beta_m$ the m th mode is always unstable.

In Fig. 8(b), we report the stability map obtained using this simplified approach (shaded area) and our numerical results (markers). The agreement between the two solutions is still reasonably good, with differences that can be attributed to the approximation we introduce in the derivation of the solution.

References

- Newman, K., Kelleher, P. E., and Smalley, Ed., 2014, "Extended Reach: Can We Reach Further?" SPE/ICoTA Coiled Tubing and Well Intervention Conference and Exhibition, The Woodlands, TX, Mar. 25–26, SPE Paper No. 168235.
- Castro, L., Craig, S., Micheli, R., and Livescu, S., 2015, "Overcoming Extended-Reach Challenges for Annular Fracturing," SPE/ICoTA Coiled Tubing and Well Intervention Conference and Exhibition, The Woodlands, TX, Mar. 24–25, SPE Paper No. 173683.
- Edillon, L., 2013, "Industry Trends Utilizing Larger Diameter Coiled Tubing for Extended Reach Operations in Northwestern Canada," SPE Annual Technical Conference and Exhibition, New Orleans, LA, Sept. 30–Oct. 2, SPE Paper No. 166401.
- Paslay, P. R., and Bogoy, D. B., 1964, "The Stability of a Circular Rod Laterally Constrained to be in Contact With an Inclined Circular Cylinder," *ASME J. Appl. Mech.*, **31**(4), pp. 605–610.
- van Adrichem, W., and Newman, K., 1993, "Validation of Coiled-Tubing Penetration Prediction in Horizontal Wells," *J. Pet. Technol.*, **45**(2), pp. 155–159.
- Kuru, E., Martinez, A., Miska, S., and Qiu, W., 2000, "The Buckling Behavior of Pipes and Its Influence on the Axial Force Transfer in Directional Wells," *ASME J. Energy Resour. Technol.*, **122**(3), pp. 129–135.
- Dawson, R., and Paslay, P. R., 1984, "Drill Pipe Buckling in Inclined Holes," *J. Pet. Technol.*, **36**(10), pp. 1734–1741.
- Mitchell, R. F., 1982, "Buckling Behavior of Well Tubing: The Packer Effect," *Soc. Pet. Eng. J.*, **22**(5), pp. 616–624.
- Chen, Y.-C., Lin, Y.-H., and Cheatham, J. B., 1990, "Tubing and Casing Buckling in Horizontal Wells," *J. Pet. Technol.*, **42**(2), pp. 140–141.
- Wu, J., and Juvkam-Wold, H. C., 1990, "Discussion of Tubing and Casing Buckling in Horizontal Wells," *J. Pet. Technol.*, **42**, pp. 1062–1063.
- Denoël, V., and Detournay, E., 2011, "Eulerian Formulation of Constrained Elastica," *Int. J. Solids Struct.*, **48**(3–4), pp. 625–636.
- Tan, X. C., and Digby, P. J., 1993, "Buckling of Drill String Under the Action of Gravity and Axial Thrust," *Int. J. Solids Struct.*, **30**(19), pp. 2675–2691.
- Fang, J., Li, S. Y., and Chen, J. S., 2013, "On a Compressed Spatial Elastica Constrained Inside a Tube," *Acta Mech.*, **224**(11), pp. 2635–2647.
- Huang, N. C., and Pattillo, P. D., 2000, "Helical Buckling of a Tube in an Inclined Wellbore," *Int. J. Nonlinear Mech.*, **35**(5), pp. 911–923.
- Sun, C., and Lukasiewicz, S., 2006, "A New Model on the Buckling of a Rod in Tubing," *J. Pet. Sci. Eng.*, **50**(1), pp. 78–82.
- Van der Heijden, G. H. M., Champneys, A. R., and Thompson, J. M. T., 2002, "Spatially Complex Localisation in Twisted Elastic Rods Constrained to a Cylinder," *Int. J. Solids Struct.*, **39**(7), pp. 1863–1883.
- Van der Heijden, G. H. M., 2001, "The Static Deformation of a Twisted Elastic Rod Constrained to Lie on a Cylinder," *Proc. R. Soc. A*, **457**(2007), pp. 695–715.
- Wicks, N., Wardle, B. L., and Pafitis, D., 2008, "Horizontal Cylinder-in-Cylinder Buckling Under Compression and Torsion: Review and Application to Composite Drill Pipe," *Int. J. Mech. Sci.*, **50**(3), pp. 538–549.
- Su, T., Wicks, N., Pabon, J., and Bertoldi, K., 2013, "Mechanism by Which a Frictionally Confined Rod Loses Stability Under Initial Velocity and Position Perturbations," *Int. J. Solids Struct.*, **50**(14–15), pp. 2468–2476.
- Miller, J. T., Su, T., Pabon, J., Wicks, N., Bertoldi, K., and Reis, P. M., 2015, "Buckling of a Thin Rod Inside a Horizontal Cylindrical Constraint," *Extreme Mech. Lett.*, **3**, pp. 36–44.
- McCourt, I., and Kubie, J., 2005, "Limits on the Penetration of Coiled Tubing in Horizontal Oil Wells: Effect of the Pipe Geometry," *Proc. Inst. Mech. Eng., Part C*, **219**(11), pp. 1191–1197.
- Zheng, A., and Sarmad, A., 2005, "The Penetration of Coiled Tubing With Residual Bend in Extended-Reach Wells," SPE Annual Technical Conference and Exhibition, Dallas, TX, Oct. 9–12, SPE Paper No. 95239, pp. 220–225.
- Bhalla, K., 1995, "Coiled Tubing Extended Reach Technology," Offshore Europe Conference, Aberdeen, UK, Sept. 5–8, SPE Paper No. 30404, pp. 392–405.
- Al Shehri, A., Al-Drweesh, S., Al Omari, M., and Al Sarakbi, S., 2007, "Case History: Application of Coiled Tubing Tractor to Acid Stimulate Open Hole Extended Reach Power Water Injector Well," SPE Asia Pacific Oil and Gas Conference, Jakarta, Indonesia, Oct. 30–Nov. 1, SPE Paper No. 110382, pp. 989–996.
- Al-Buali, M. H., Dashash, A. A., Shawly, A. S., Al-Guraini, W. K., Al-Drweesh, S. M., Bugrov, V., and Nicoll, S., 2009, "Maximizing Coiled Tubing Reach During Logging of Extended Horizontal Wells Using E-line Agitator," Kuwait, International Petroleum Conference and Exhibition, Kuwait City, Kuwait, Dec. 14–16, SPE Paper No. 127399, pp. 324–334.
- Wicks, N., Pabon, J., and Zheng, A., 2014, "Modeling and Field Trials of the Effective Tractor Force of Axial Vibration Tools," Galveston, TX, Sept. 10–11, SPE Paper No. 170327.
- McLachlan, N. W., 1951, *Theory and Applications of Mathieu Functions*, Oxford Press, London.
- Markevich, N. I., and Sel'kov, E. E., 1989, "Parametric Resonance and Amplification in Excitable Membranes. The Hodgkin–Huxley Model," *J. Theor. Biol.*, **140**(1), pp. 27–38.
- Huseyin, K., and Lin, R., 1991, "An Intrinsic Multiple-Time-Scale Harmonic Balance Method for Nonlinear Vibration and Bifurcation Problems," *Int. J. Nonlinear Mech.*, **26**(5), pp. 727–740.
- Mettler, E., 2014, "Stability and Vibration Problems of Mechanical Systems Under Harmonic Excitation," *Dynamic Stability of Structures*, Pergamon Press, New York, pp. 169–188.
- Stephenson, A., 1908, "On a New Type of Dynamic Stability," *Mem. Proc. Manchester Lit. Philos. Soc.*, **52**(8), pp. 1–10.
- Stephenson, A., 1908, "On Induced Stability," *Philos. Mag.*, **15**(86), pp. 233–236.
- Mathieu, E., 1868, "Mémoire sur le Mouvement Vibratoire d'une Membrane de Forme Elliptique," *J. Math. Pures Appl.*, **13**, pp. 137–203.
- Arscott, F. M., 1964, *Periodic Differential Equations. An Introduction to Mathieu, Lamé, and Allied Functions*, The MacMillan Company, New York.
- McLachlan, N. W., 1947, *Theory and Application of Mathieu Functions*, Clarendon Press, Oxford, UK.
- Mitchell, J., "Techniques for the Oscillated Pendulum and the Mathieu Equation," <http://www.math.ou.edu/npetrov/joe-report.pdf>
- Birdsall, C. K., and Langdon, A. B., 1985, *Plasma Physics Via Computer Simulations*, McGraw-Hill, New York.
- Timoshenko, S. P., and Gere, J. M., 1961, *Theory of Elastic Stability*, 2nd ed., McGraw-Hill Book, New York.
- Pabon, J., Wicks, N., Chang, Y., Dow, B., and Harmer, R., 2009, "Modeling Transient Vibrations While Drilling Using a Finite Rigid Body Approach," First International Colloquium on Nonlinear Dynamics of Deep Drilling Systems, Galveston, TX, Oct. 5–6, SPE Paper No. 137754, pp. 83–87.
- Budyans, R., and Young, W., 2001, *Roark's Formulas for Stress & Strain*, 7th ed., McGraw-Hill, New York.
- Antman, S. S., 1995, *Nonlinear Problems of Elasticity*, Springer, Berlin.
- Coleman, B. D., Dill, E. H., Lembo, M., Lu, Z., and Tobias, I., 1993, "On the Dynamics of Rods in the Theory of Kirchhoff and Clebsch," *Arch. Rational Mech. Anal.*, **121**(4), pp. 339–359.
- Hill, G. W., 1886, "On the Part of the Motion of the Lunar Perigee Which is a Function of the Mean Motions of the Sun and Moon," *Acta. Math.*, **8**(1), pp. 1–36.
- Lee, T. C., 1976, "A Study of Coupled Mathieu Equations by Use of Infinite Determinants," *ASME J. Appl. Mech.*, **43**(2), pp. 349–352.
- Zounes, R. S., and Rand, R. H., 1998, "Transition Curves for the Quasi-Periodic Mathieu Equation," *SIAM J. Appl. Math.*, **58**(4), pp. 1094–1115.
- Simakhina, S., 2003, "Stability Analysis of Hill's Equation," Master thesis, University of Illinois at Chicago, Chicago, IL.
- Ruby, L., 1995, "Applications of the Mathieu Equation," *Am. J. Phys.*, **64**(1), pp. 39–44.